Electrostatic Coupling and Identification of Single-Defects in GaN/AlGaN Fin-MIS-HEMTs

A. Grill[b,*], B. Stampfer[a,b], Ki-Sik Im[d], J.-H. Lee[e], C. Ostermaier[c], H. Ceric[b], M. Waltl[a,b], T. Grasser[b]

[a] Christian Doppler Laboratory for Single-Defect Spectroscopy in Semiconductor Devices at the Institute for Microelectronics, TU Wien, Vienna, Austria
[b] Institute for Microelectronics, TU Wien, Vienna, Austria
[c] Infineon Technologies AG, Villach, Austria
[d] Advanced Material Research Center, Kumoh National Institute of Technology, Gumi, Gyeongbuk, Republic of Korea
[e] School of Electronics Engineering, Kyungpook National University, Daegu, Republic of Korea

ARTICLE INFO

ABSTRACT

Charge trapping effects are considered as one of the most severe reliability issues in gallium nitride (GaN)/ aluminium gallium nitride (AlGaN) metal-insulator-semiconductor HEMTs (MISHEMTs). Thus, the identification of the origin and the physical properties of active defects is one of the key factors to improve the stability of GaN technology. In this work, we suggest two neighboring nitrogen vacancies as the origin of correlated random telegraph noise (RTN) emissions in a GaN/AlGaN fin-MISHEMT. We determine the magnitude of electrostatic coupling between these two defects by using three different approaches and verify the results by simulating the RTN emissions of a similar system using a Hidden Markov Model (HMM).

1. Introduction

In recent years, GaN/AlGaN high-electron-mobility transistor (HEMTs) were found to be one of the most promising alternatives to silicon power transistors. This is mainly because of the favorable electronic properties of the material system, where high electron mobilities together with high breakdown fields allow to design devices which are smaller, faster and at the same time more efficient compared to silicon at a certain power level [1]. One promising approach to create normally-off devices is the creation nano-sized fin-MIS-HEMT structures, where geometric scaling of the channel allows to engineer V_{th} without changing the properties of the barrier layer [2,3].

Despite all recent improvements in GaN technology, charge trapping is still the major performance limiting reliability issue for many device topologies. Therefore, the identification of the physical properties of defects is a key factor for the improvement of GaN power devices. However, the very high defect densities together with the rather complicated electrostatics makes experimental defect characterization extremely challenging.

The first reason for these complications is that measurements on large-area devices will always contain a large number of different kinds of defects, which obfuscates the electrical response of a certain type. Additional complications in the analysis of individual defect properties are caused by broad distributions of capture and emission times [4,5]

and charge feedback effects observed in large area devices [6].

In our previous study [7], we extracted single-defect properties from the RTN emissions of a 50 nm × 1 µm fin-MIS-HEMT [2,3]. We will now use these results to determine the most likely defect candidate to produce such signals. Since in our previous work, we concluded that the correlated RTN stems from two neighboring defects, we will calculate the required coupling factors between two neighboring defects and verify the results by comparing them to simulated emissions from a similar defect structure with different coupling factors.

2. Experimental

A schematic of the probed device can be seen in Fig. 1. It consists of a 30 nm thick AlGaN barrier (30% Al) on top of a 80 nm GaN channel layer and a 2 µm thick highly resistive GaN buffer grown on a sapphire substrate. After the formation of the fin structure, the metal gate-stack (Ni/Au) was formed on top of a 20 nm Al_2O_3 gate oxide, see [2,3] for device details. The RTN measurements were performed using our TDDS measurement instrument (TMI) and converted to ΔV_{th} using the transfer-characteristics of the device shown in Fig. 2 [8]. The large trap density together with the large-area parasitic metal-oxide-semiconductor field-effect transistor (MOSFET) in our device generate a considerable amount of 1/f noise in the drain-source current, thereby obscuring charge transition events of single-defects with small step
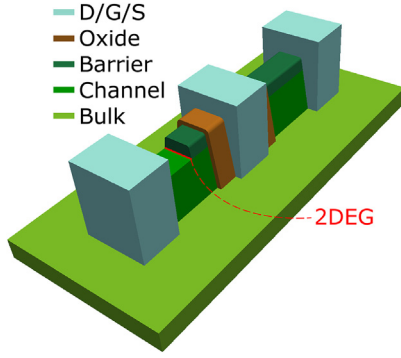
---

* Corresponding author.
  E-mail address: grill@iue.tuwien.ac.at (A. Grill).

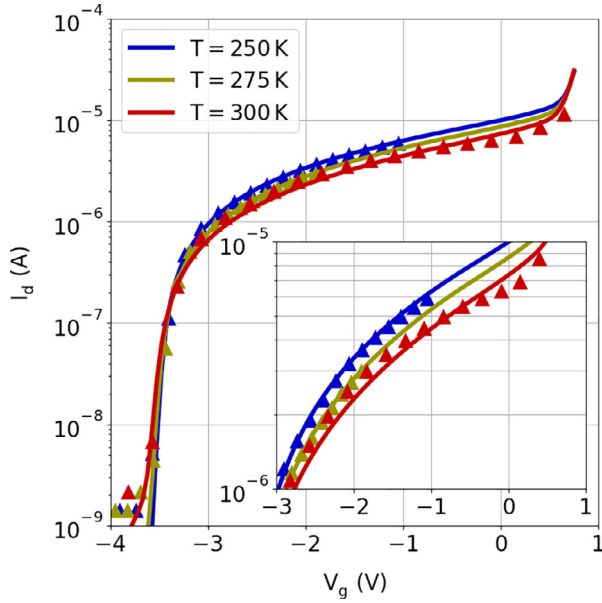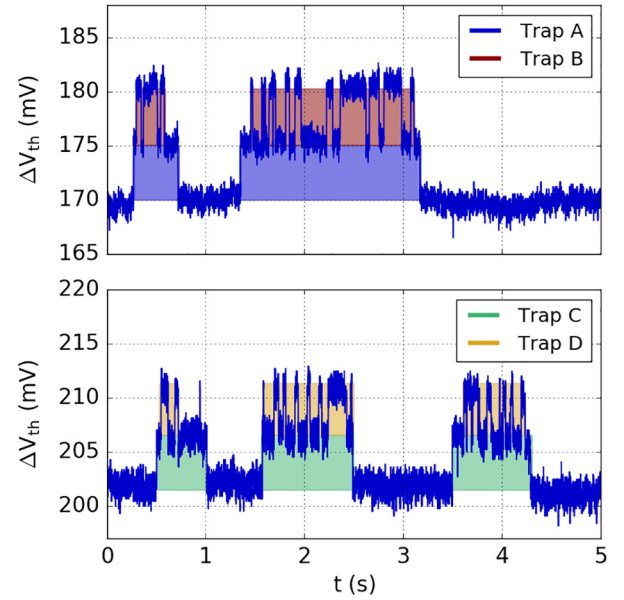Fig. 1. Schematic pictures of the GaN/AlGaN fin MIS-HEMTs used in our experiments. In contrast to silicon devices, where the inversion channel is concentrated at the oxide interface, in these devices the channel lies at the channel/barrier interface.


Fig. 2. The transfer characteristics of the device at different temperatures. Since the measurements needed to be done on the same device, the curves were corrected by the accumulated stress-related BTI drift. The kink in the accumulation region is attributed to the turn-on of the parasitic bulk-MOS transistor [3]. For the TCAD simulations we used the device simulator Minimos-NT [10].

Fig. 3. The equivalent ΔV_{th} values of the recorded RTN signals were calculated from the $I_d(V_g)$ characteristics of the device. Defects 'B' and 'D' are only active if the slower traps 'A' and 'C' have captured an electron. Their similar step heights together with the correlated behaviour indicate that the traps are in immediate vicinity to each other. Note that a median filter was applied to the data for illustration purposes. The sampling frequency for all measurements was 10 kHz with a drain bias of 50 mV. The traces shown were recorded at $V_g = -1.45$ V (upper) and $V_g = -0.775$ V (lower) (from [7]).
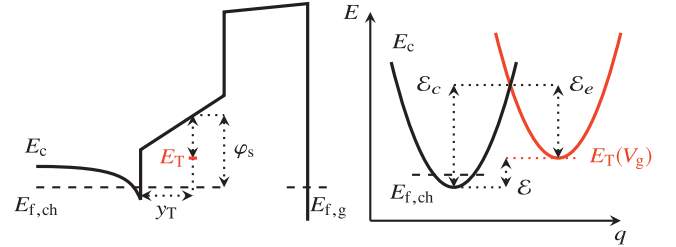
Fig. 4. Left: The schematic conduction band diagram of the fin-MIS-HEMT structure along a vertical cut through the gate with the extracted quantities. Right: A schematic representation of the adiabatic potential energy surface of a two-state NMP defect with equal curvatures. A linear relationship between the trap level and the applied gate voltage is obtained as long as band-bending in the barrier layer can be neglected (from [7]).

heights [7].

The measurements were conducted at different cryogenic temperatures to reduce the number of active defects and also to limit thermal noise. If many different defects are active in time-dependent defect spectroscopy (TDDS) measurements [9], the probability of multiple defects with similar step heights emitting at similar times is increased. As a consequence, the accuracy of the mapping of individual emission events to distinct defect clusters is impaired. Additionally, any continous bias temperature instability (BTI) drift of the device under test during the RTN measurements would change the effective gate bias seen by the device, which would make it much more difficult to extract the correct voltage dependence of the defects. For these reasons, RTN measurements were used because only a small number of defects were actively switching at the same time. Despite the tough measurement conditions, we were able to show four dominant defects producing RTN. Typical signals produced by these defects for a temperature $T = 200$ K can be seen in Fig. 3. The most interesting observation here is the activity of defects 'B' and 'D', which appears to be triggered by the two slower traps 'A' and 'C'. With other words, the emissions of the fast defects always start when the slower defects capture a charge and stop

as soon as their charge is again emitted.

3. Extraction of the Defect Parameters

The voltage dependence of the characteristic time constants of the defects at different temperatures was extracted by the spectral method presented in [7]. The results can be seen in Fig. 5. The correlated charge trapping behavior of the two defect-pairs ('AB' and 'CD') implies a strong electrostatic coupling between them. Furthermore, the similar step heights of the defects and their similar voltage dependence indicate that the defects pairwise reside in close proximity to each other. On top of that, their similar intersection points also point to similar trap levels.

The defect parameters were obtained from a two-state non-radiative multi-phonon (NMP) model as shown in Fig. 4. The calculation of the parameters thereby relies upon the voltage dependence of the capture and emission barriers $\mathcal{E}_c$ and $\mathcal{E}_e$:

$$k_B T \frac{\partial \ln(\tau_{c,e})}{\partial V_g} = \frac{\partial \mathcal{E}_{c,e}}{\partial V_g} \tag{1}$$
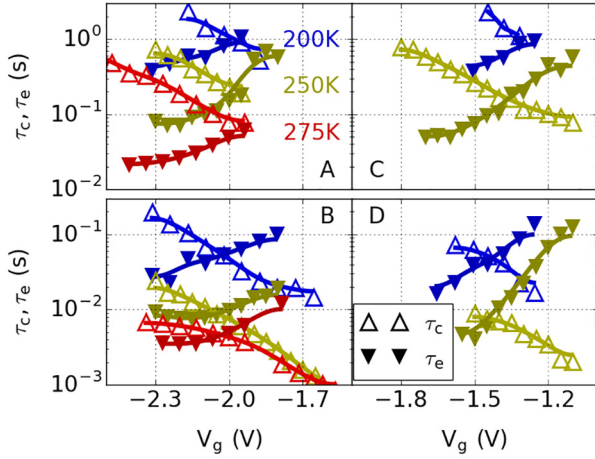
Fig. 5. The extracted capture and emission times share the same intersection points and bias dependence, suggesting a strong coupling between them. Their rather weak slopes point to a defect location in the barrier close to the channel (from [7]).

The trap level shift for a certain gate voltage is given by the difference of the capture and emission barriers (see Fig. 4). This fact can be used to express the voltage dependence of the capture and emission times in terms of the voltage dependence of the surface potential φ_s [7].

$$\frac{\partial \mathcal{E}}{\partial V_g} = \frac{\partial \mathcal{E}_c}{\partial V_g} - \frac{\partial \mathcal{E}_e}{\partial V_g} = \frac{\partial \varphi_s}{\partial V_g} \tag{2}$$

With the thickness of the barrier t_{bar} and the permittivities of the barrier and the oxide, ε_{bar} and ε_{ox}, the vertical defect position is given by [7]

$$y_{trap} = \left(t_{bar} + t_{ox} \frac{\varepsilon_{bar}}{\varepsilon_{ox}} \right) \frac{\partial \mathcal{E}}{\partial V_g}. \tag{3}$$

The trap-level is then calculated from the intersection points of τ_c and τ_e (i.e. where $E_{f,ch} = E_T$), which are converted into an equivalent shift of the trap-level at the position y_{trap} of the defect. The remaining quantities like the surface potential $\varphi_{s,0}$ and the band offset of the AlGaN layer at the hetero-interface φ_{ch} were taken from technological computer aided design (TCAD) simulations [7,10].

$$E_T = \frac{\partial \varphi_s}{\partial V_g} V_{g,int} + \left(\varphi_{s,0} - \varphi_{ch} \right) \frac{y_{trap}}{t_{bar}} + \varphi_{ch}. \tag{4}$$

The temperature activation of the process was calculated from the Arrhenius equation for the capture and emission times at the intersection point of τ_c and τ_e (not shown, see [7]). Within the strong phonon-electron coupling regime ($\mathcal{E}_R \gg \mathcal{E}$) and for equal curvatures of the two states, the apparent activation energy of an NMP process can be calculated from the NMP barriers $\mathcal{E}_{c,e}$ and the relaxation energy $\mathcal{E}_R$ [9,11]:

$$\mathcal{E}_c \approx \frac{1}{4}\mathcal{E}_R + \frac{1}{2}\mathcal{E}, \quad \mathcal{E}_e \approx \frac{1}{4}\mathcal{E}_R - \frac{1}{2}\mathcal{E}, \tag{5}$$

Eq. (5) shows that for strong electron-phonon coupling, the apparent activation energy of the process is dominated by the relaxation energy $\mathcal{E}_R \approx 4\mathcal{E}_A$ of the NMP process. The resulting parameters in Table 1 shows that the extracted vertical trap positions of the correlated traps are in close proximity to each other. Moreover, they also share the same trap level because their intersection points also match very closely. This is despite of their absolute time constants differing by at least one order of magnitude. One explanation for all of the observed behavior, namely (i) the correlated RTN behavior, (ii) the similar trap levels and (iii) the similar voltage behavior, can be the local potential energy surface seen by the defects 'B' and 'D', which obviously changes if defects 'A' and 'C' capture a charge.

The changes in the local potential, therefore, induce an electrostatic

Table 1
The extracted defect properties from Fig. 5. The vertical trap positions together with the similar trap levels show that the correlated trap pairs 'AB' and 'CD' are in close proximity to each other. All of the extracted parameters, the similar intersection points and voltage dependence and their correlated behavior suggest that the electrostatic potential around defects 'B' and 'D' changes with defects 'A' and 'C' having captured an electron (from [7]).

Trap	y_{trap} (nm)	E_T (eV)	k_0 (s^{-1})	E_R (eV)
A	6.7	0.63	1.1×10^7	0.63
B	5.8	0.59	5.5×10^9	0.61
C	9.2	0.68	7.3×10^6	0.59
D	9.8	0.72	5.2×10^9	0.62
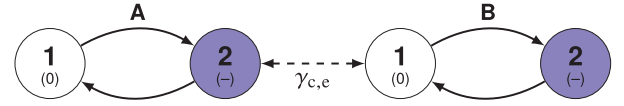
Fig. 6. The structure of a system of two coupled two-state defects used in the HMM simulations. The capture and emission rates of defect A change by γ_c and γ_e if defect B captured a charge.

coupling between those defects, where the charge state of one defect influences the capture and emission times of the other defect. The structure of such a system of defects can be seen in Fig. 6. Naturally, the question arises on whether the assumption of looking at a signal from two correlated pairs of traps can be further confirmed or if the observed RTN emissions require unrealistically high coupling factors. In the next sections, we will investigate how to model the electrostatic coupling between two defects and estimate the necessary coupling factors to obtain signals comparable to Fig. 3.

## 4. Electrostatic Coupling of Defects

The electrostatic coupling between two independent defects is often modeled as a shift of the local potential due to the Coulomb potential of a single point charge [12–15]. The perturbation of the local potential of one defect thereby can act on the other one in two different ways. One is a shift of the initial trap level induced by the additional local Coulomb barrier. The other one is a remote mechanism, where two distant traps lie on the same percolation path [16,17].

Because the coupling of the time constants seems to be rather large in this case, most likely the first mechanism dominates. This is mainly because the additional Coulomb barrier enters the rates exponentially and the supply of carriers (i.e. the percolation path) only linearly. Other arguments speaking against a lateral separation of the coupled defects are their similar step heights (i.e. trap depths) as well as the bias region they were observed at. The influence of the percolation path would be strongest at weak channels for voltages around threshold voltage (V_{th}), however, the experiments were conducted at bias conditions quite far from that value.

The magnitude of the potential perturbation and thus the trap level shift caused by a nearby trap is hard to predict if only classical or semi-classical simulations are available. One obvious approach is to treat defects as point charges and add them to the discretized Poisson equation. Another approach is the well-known equation for the analytic Coulomb potential, which is inversely proportional to the distance to the charge. With r being the distance to the charge:

$$\varphi = -\frac{q_0}{4\pi\varepsilon_0\varepsilon_r r} \tag{6}$$

The numerical and analytical solutions for the potential of a point charge in three dimensions are depicted in Fig. 7. With sufficiently fine grids, the near-field impact of a single charge is overestimated whereas
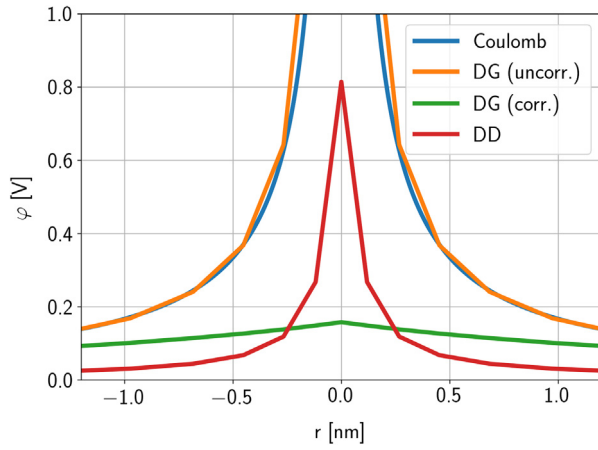
Fig. 7. The numerical and analytical solutions of a point charge in lightly doped GaN at $r = 0$ in three dimensions. drift-diffusion (DD) simulations are known to predict unphysical charge crowding for low grid-spacing. To overcome this problem and to be independent of grid spacing, a first order quantum correction model like the density gradient (DG) model or other corrections like the Conwell-Weisskopf model can be used.

the far-field impact is underestimated. A first-order quantum correction model like the density gradient (DG) model [18–20] or empirical models like the Conwell-Weisskopf model [21] can be used to mitigate this problem and also make the numerical solution independent of grid spacing. Another recent approach makes use of an analytical expression for the short-range force acting on a particle at a distance r from the charge. It resembles the Coulomb force for large distances whereas at short distances it decreases to zero, removing the singularity and rapidly changing components [22]:

$$E(r) = \frac{q_0 r}{4\pi\varepsilon (r^2 + 0.5 r_c^2)^{3/2}}$$ (7)

The force term has its maximum at the cutoff radius r_c and then decreases monotonically towards the point of the charge. According to [15], the value of the cutoff radius should be chosen to be at the effective Bohr radius of the ground state of a donor. For AlGaN it can be calculated by

$$r_c = \frac{4\pi\hbar^2\varepsilon_0\varepsilon_r}{m_e^* q_0^2} = 1.75 \text{ nm},$$ (8)

with $\varepsilon_r = 8.6$ being the relative permittivity and $m_e^* = 0.26 m_e$ the relative electron mass of AlGaN. The local potential change and thus the local shift of the trap energy can easily be derived by integrating (7).

$$\varphi(r) = -\frac{q_0}{4\pi\varepsilon_0\varepsilon_r \sqrt{2r^2 + r_c^2}}$$ (9)

A straightforward way to check the validity of the solution provided in (9) is to compare it to the quantum mechanical solution for the ground state of a hydrogen atom with an effective Bohr radius as given in (8). The derivation of the potential is based on the radial-symmetric charge density of an electron in the ground state given by

$$\rho(r) = q_0 |\psi_{100}|^2 = \frac{q_0}{\pi r_c^3}\exp\left(-\frac{2r}{r_c}\right).$$ (10)

The magnitude of the electric field of the electron cloud is then found by applying Gauss' law with a spherical ansatz:

$$|E(r)| = \frac{q_0}{4\pi\varepsilon_0\varepsilon_r r^3}\left[1 - \exp\left(-\frac{2r}{r_c}\right)\left(1 + \frac{2r}{r_c} + \frac{2r^2}{r_c^2}\right)\right]$$ (11)

Finally, the potential of the electron can easily be calculated from the electric field by integration of (11).
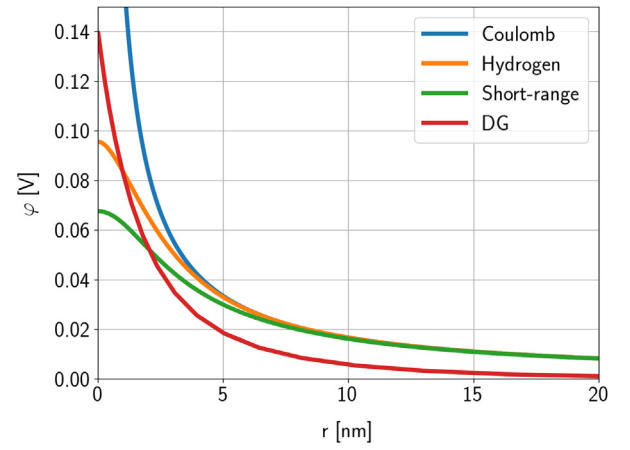
Fig. 8. The results of the quantum corrected drift-diffusion simulations versus the analytic short-range potential used in [22] and the solution of the Hydrogen model. The two analytic potentials match very well and converge towards the solution of the Coulomb potential at larger distances. The difference to the numerical solution can most likely be explained by the fact that the simulations were conducted in semi-insulating GaN while the analytical solutions assume insulators.

$$\varphi(r) = \frac{q_0}{4\pi\varepsilon_0\varepsilon_r}\left[\frac{\exp\left(-\frac{2r}{r_c}\right) - 1}{r} + \frac{\exp\left(-\frac{2r}{r_c}\right)}{r_c}\right]$$ (12)

The results of these analytic potentials versus the corrected numerical solution from Fig. 7 can be seen in Fig. 8. The rather large difference between the analytical solution and the numerical solution can be explained for two reasons. The first one is additional screening due to the lightly doped semiconductor, whereas the analytic solutions assume ideal insulators. The second and probably more important one is the lack of a well-calibrated set of simulation parameters for the density gradient model for point defects in GaN, which would likely require first-principle simulations based on assumptions on the atomistic structure of the defect.

5. Results and Discussion

In order to calculate the actual potential shift from the results in Fig. 8, the distance between the two defects has to be determined. The vertical defect positions extracted in Table 1 unfortunately cannot be used because the lateral distance between the traps is unknown. Thus, the only way to estimate the coupling factors is to choose a suitable defect candidate based on the extracted trap levels. Fig. 9 lists the most common trap levels of native defects in GaN [23].

Given the similar lattice structures of the two materials, the energy levels of the defects probably can also be taken directly for AlGaN. It should be noted that this can only be valid if the extracted energies in Fig. 9 are on an absolute energy scale and the effects of lattice strain on the defects are neglected.

Because of the vertical positions, the barrier can be identified as the segment where the defects are located. TCAD simulations in Minimos-NT [10] show that the conduction band minimum in the AlGaN barrier is at approximately 3.7 eV for $V_g = 0$ V. If the same absolute energy levels like in GaN are assumed for defects in the barrier, the most likely defect candidates turn out to be either a dislocation or a nitrogen vacancy. Note that in the case of a defect in the barrier, the energy levels in Fig. 9 shifted by the conduction band offset between GaN and AlGaN. Since the nitrogen vacancy is one of the most common native defects in GaN and also likely to be responsible for the observed n-type conduction, for the following extraction of the coupling factors, it is chosen as the most likely defect candidate. Furthermore, because of the similar trap levels of the two coupled defect pairs, the best guess is to make a
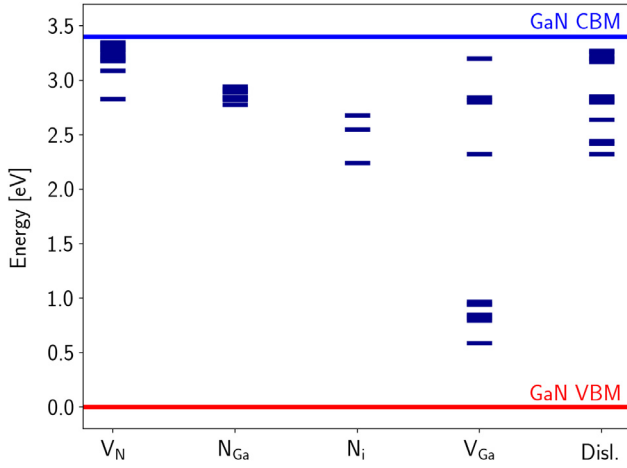
Fig. 9. The energy levels formed by intrinsic point defects, extended defects, and their complexes. The listed defects are the nitrogen vacancy (V_N), the nitrogen antisite (N_{Ga}), the nitrogen interstitial (N_i), the gallium vacancy (V_{Ga}), and various extended dislocation-type defects. The red and blue lines are the valence and conduction band edges in GaN (data taken from [23]). (For interpretation of the references to colour in this figure legend, the reader is referred to the web version of this article.)

Fig. 10. The distance between two potential nitrogen vacancy sites in an ideal crystal structure of AlGaN. The first nitrogen vacancy is depicted with the light-blue atom in the center of the picture. The border of the grey region marks the minimum distance to the first nitrogen-site not sharing the same gallium atom with the initial defect. The minimum distance between two nitrogen vacancies not sharing the same Ga atom is approximately 5 Å.

worst-case assumption by assuming the very same type of defect in a nearest neighborhood manner. The minimum distance between two nearest neighbor nitrogen vacancies can be calculated from an undistorted crystal structure with the lattice constants a and c of the AlGaN barrier. It should be noted that the two nitrogen vacancies forming a defect pair should not share one Ga atom. Such defects would probably distort the overall crystal structure too much and thus are probably not going to be stable. The lattice constants of wurtzite AlGaN alloy can theoretically be calculated based on their alloy composition x [24]:

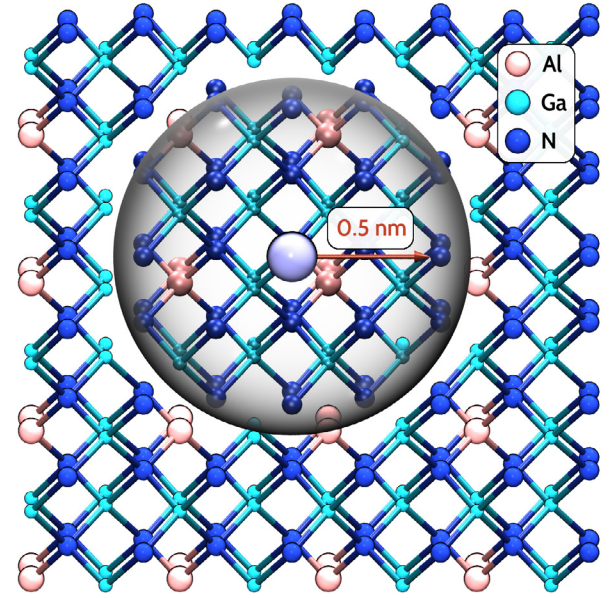$$a_{Al_xGa_{1-x}N} = (3.1986 - 0.0891x)\ \text{Å} \tag{13}$$

$$c_{Al_xGa_{1-x}N} = (5.2262 - 0.2323x)\ \text{Å} \tag{14}$$

The lattice constants of the investigated devices are calculated to $a = 3.172$ Å and $c = 5.157$ Å. From the crystal structure in Fig. 10 it can be seen that the worst-case distance between two nitrogen sites not sharing the same Ga atom is around 5 Å. Therefore, the second nearest defect would have a distance of approximately 10 Å.

Table 2 lists the resulting energy shifts for those defects, which can easily be translated into coupling factors using the Arrhenius law for the appropriate temperatures.

$$\gamma = \exp\left(\frac{\Delta E_T}{k_B T}\right) \tag{15}$$

The results of the calculated energy shifts are shown in Table 3. The values for the unscreened analytic Coulomb potential can be safely neglected because of its unrealistic values for distances very close to the point charge (see (6)). Therefore, realistic coupling factors are in the range of ∼ 15–∼ 500. It should be said that because a structural defect in reality will always cause changes in the local configuration of atoms (and thus their bonding lengths), the provided results should still be seen as a rather coarse approximation. On top of that, the hydrogen model and the calculation of the critical radius in (8) are somewhat crude simplifications of the real local potential energy surface, which can only be provided by first principle simulations. The results, however, allow quantifying a range of realistic coupling factors that could be present in a worst-case scenario. After estimating a range of realistic coupling factors for neighboring defect sites, the coupling factors required to observe correlated RTN signals similar to Fig. 3 need to be found. In order to do that, we used a HMM library which was

Table 2

The trap energy shifts calculated for the first and second-nearest defect site of nitrogen vacancies with the potentials in Fig. 8. While the Coulomb potential and the DG model predict rather large difference between the two different defects, the potentials of the hydrogen model and the short-range model only show a quite weak distance dependence.

| Model	ΔE_T	
	0.5 nm	1 nm
Coulomb	335 meV	167 meV
Hydrogen	92 meV	84 meV
Short-range	66 meV	63 meV
DG	105 meV	83 meV

Table 3

The coupling factors of the two nitrogen vacancies for the three different temperatures. Realistic coupling factors are in the range of ∼ 15 to ∼ 500 because the values of the unscreened Coulomb potential can be safely neglected.

	γ (0.5 nm)			γ (1 nm)		
	200 K	250 K	275 K	200 K	250 K	275 K
Coulomb	2.76×10^8	5.67×10^6	1.38×10^6	16152	2326	1150
Hydrogen	208	72	49	131	49	35
Short-range	46	21	16	39	19	14
DG	442	131	84	123	48	33

specifically written to simulate RTN emissions of single-defects by our group. It is used to simulate a coupled pair of defects with the time constants taken from Fig. 5 for different coupling factors. A system consisting of two coupled two-state defects (see Fig. 6) can be derived from two two-state defects 'A' and 'B' with the transition matrices

$$\underline{k}_A = \begin{bmatrix} 1 - k_{12}^A & k_{12}^A \\ k_{21}^A & 1 - k_{21}^A \end{bmatrix}, \tag{16}$$
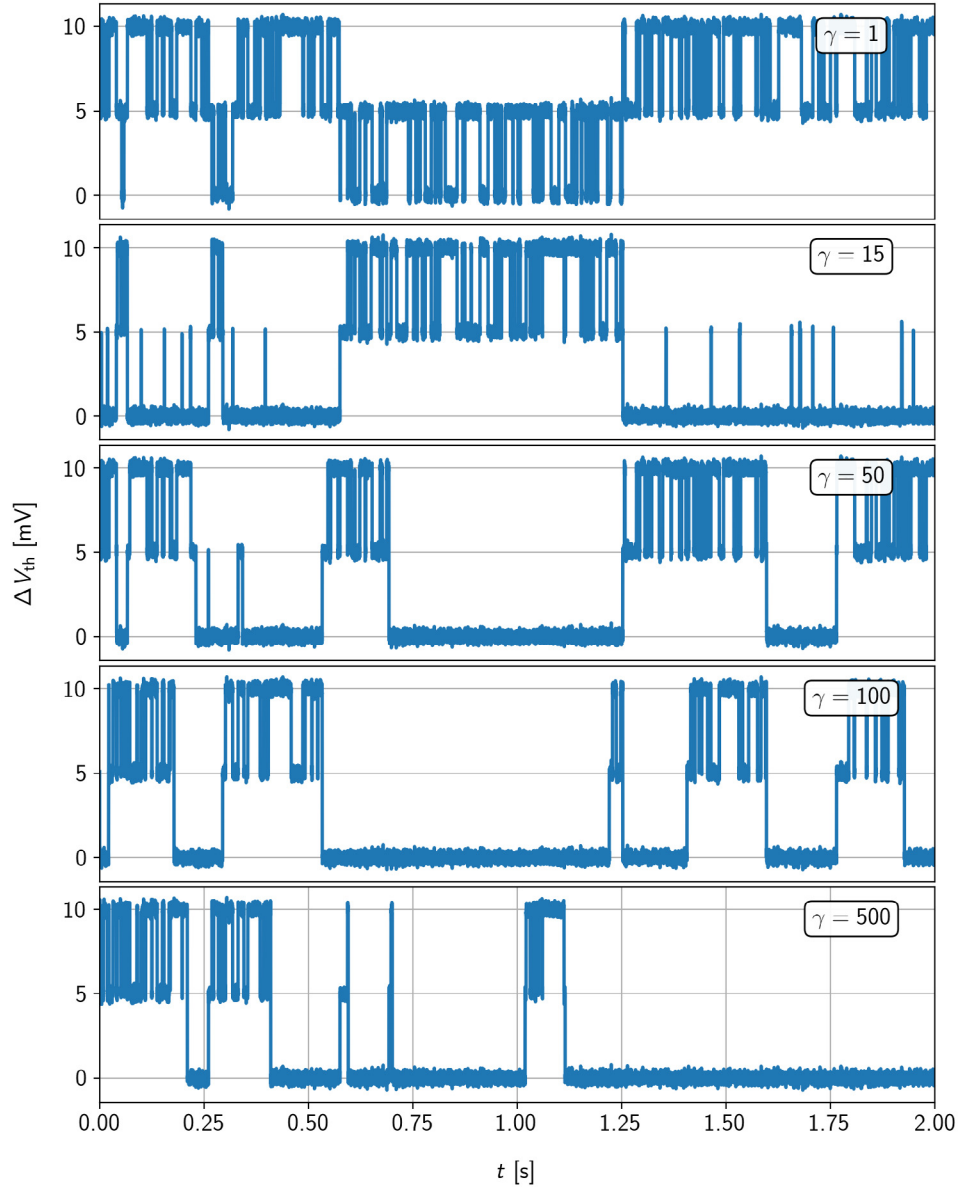
Fig. 11. Simulation results for the proposed system of two coupled two-state defects with different coupling factors. The time constants were taken from Fig. 5 for a gate voltage of −1.95 V and a temperature of 250 K. The sampling frequency was chosen to be 10 kHz according to the measurements. It can be seen that a coupling factor of about $\gamma = 100$ is needed in order to reliably suppress the modified RTN signa.l of defect 'B'.

$$\underline{\boldsymbol{k}}_{\mathrm{B}} = \begin{bmatrix} 1 - k_{12}^{\mathrm{B}} & k_{12}^{\mathrm{B}} \\ k_{21}^{\mathrm{B}} & 1 - k_{21}^{\mathrm{B}} \end{bmatrix}. \tag{17}$$

The transition matrix of the combined system is then given by the Kronecker product of the two individual defects [25]:

$$\underline{\boldsymbol{k}} = \begin{bmatrix} (1 - k_{12}^{\mathrm{A}}) \cdot \underline{\boldsymbol{k}}_{\mathrm{B}} & k_{12}^{\mathrm{A}} \cdot \underline{\boldsymbol{k}}_{\mathrm{B}} \\ k_{21}^{\mathrm{A}} \cdot \underline{\boldsymbol{k}}_{\mathrm{B}} & (1 - k_{21}^{\mathrm{A}}) \cdot \underline{\boldsymbol{k}}_{\mathrm{B}} \end{bmatrix} \tag{18}$$

If now, for example, defect A captures an electron, because of the coupling, the capture and emission rates of defect B change. The modified transition matrix of defect B with the coupling factors γ_{c} and γ_{e} then is:

$$\underline{\boldsymbol{k}}_{\mathrm{B}}' = \begin{bmatrix} 1 - \gamma_{\mathrm{c}} k_{12}^{\mathrm{B}} & \gamma_{\mathrm{c}} k_{12}^{\mathrm{B}} \\ \gamma_{\mathrm{e}} k_{21}^{\mathrm{B}} & 1 - \gamma_{\mathrm{e}} k_{21}^{\mathrm{B}} \end{bmatrix} \tag{19}$$

The modified transition matrix has then to be inserted into (18) for the states where A has captured an electron. The transition matrix of the

coupled system then becomes:

$$\underline{\boldsymbol{k}} = \begin{bmatrix} (1 - k_{12}^{\mathrm{A}}) \cdot \underline{\boldsymbol{k}}_{\mathrm{B}} & k_{12}^{\mathrm{A}} \cdot \underline{\boldsymbol{k}}_{\mathrm{B}} \\ k_{21}^{\mathrm{A}} \cdot \underline{\boldsymbol{k}}_{\mathrm{B}}' & (1 - k_{21}^{\mathrm{A}}) \cdot \underline{\boldsymbol{k}}_{\mathrm{B}}' \end{bmatrix} \tag{20}$$

To derive the required coupling factors, we shall define what it means if the emissions of defect 'B' cannot be measured when defect 'A' is empty (i.e. the correlated behavior). For a fixed sampling time this requires the mean time-to-emission of 'B' to be approximately one order of magnitude below the time resolution of the measurement because of the stochastic nature of the process.

The results of the RTN simulations for different coupling factors can be seen in Fig. 11 for a sampling rate of 10 kHz, a gate voltage of −1.95 V, and a temperature of 250 K. Because the same sampling rate was also used for the measurements, a coupling factor of about $\gamma = 100$ is needed to reliably suppress the emissions of 'B' in the ground state of 'A'. This is already at the upper limit of the calculated factors in Table 3, however, given the uncertainties in the derivation of the time constants and the perturbation potentials for the coupling factors, the result is still

well in range for the nearest-neighbor nitrogen vacancy.

Literature on single defect studies suggests that coupling factors between 10 and 20 seem to be realistic for strongly coupled defects [26,16,27,28]. Unfortunately, they do not provide the temperature which was used during their measurements. Quite interestingly, the provided coupling factors calculated for 300 K and 1 nm are in the range from ~ 11 to ~ 25 for the last three models in Table 3, closely matching their observations.

6. Conclusions

Based on the results of our previous investigation on single-defect properties of a nanoscale fin-MIS-HEMT device, we suggested two neighboring nitrogen vacancies as the most likely defect candidates to cause the correlated RTN emissions in our measurements. We calculated realistic electrostatic coupling factors for those two defects being in close vicinity to each other. We first estimated the potential perturbations caused by a neighboring defect capturing a charge. To confirm the results, we used a HMM to study the RTN emissions of a coupled pair of two-state defects with different coupling factors. The results also suggest that the coupling between both of the evaluated defect candidates is well in range to other studies on the same topic. Thus, we stipulate that the observed correlated RTN was most likely caused by two neighboring nitrogen vacancies in the barrier of the device.

Acknowledgment

References

[1] Kaminski N, Hilt O. SiC and GaN devices-competition or coexistence? 2012 7th International Conference on Integrated Power Electronics Systems (CIPS). 2012. p. 1–11.

[2] Im K-S, Kang H-S, Lee J-H, Chang S-J, Cristoloveanu S, Bawedin M, et al. Characteristics of GaN and AlGaN/GaN FinFETs. Solid- State Electron 2014;97:66–75. https://doi.org/10.1016/j.sse.2014.04.033.

[3] Im K-S, Kang H-S, Kim D-K, Vodapally S, Park Y, Lee J-H, et al. Temperature-dependent characteristics of AlGaN/GaN FinFETs with sidewall MOS channel. Solid-State Electron 2016;120:47–51. https://doi.org/10.1016/j.sse.2016.03.007.

[4] Lagger P, Reiner M, Pogany D, Ostermaier C. Comprehensive study of the complex dynamics of forward bias-induced threshold voltage drifts in GaN Based MIS-HEMTs by stress/recovery experiments. IEEE Trans Electron Dev 2014;61(4):1022–30. https://doi.org/10.1109/TED.2014.2303853.

[5] Ostermaier C, Lagger P, Reiner M, Pogany D. Review of bias-temperature instabilities at the III-N/dielectric interface. Microelectron Reliab Mar. 2018;82:62–83. https://doi.org/10.1016/J.MICROREL.2017.12.039.

[6] Grill A, Rzepa G, Lagger P, Ostermaier C, Ceric H, Grasser T. Charge feedback mechanisms at forward threshold voltage stress in GaN/AlGaN HEMTs. 2015 IEEE International Integrated Reliability Workshop IEEE; 2015. p. 41–5. https://doi.org/10.1109/IIRW.2015.7437064.

[7] Grill A, Stampfer B, Waltl M, Im K-S, Lee J-H, Ostermaier C, et al. Characterization and modeling of single defects in GaN/AlGaN fin- MIS-HEMTs. 2017 IEEE International Reliability Physics Symposium IEEE; 2017. https://doi.org/10.1109/IRPS.2017.7936285. 3B-5.1-3B-5.5.

[8] Waltl M, Grill A, Rzepa G, Goes W, Franco J, Kaczer B, et al. Nanoscale evidence for the superior reliability of SiGe high-k pMOSFETs. 2016 IEEE International Reliability Physics Symposium (IRPS) 2016. https://doi.org/10.1109/IRPS.2016.7574644. XT-02-1-XT-02-6.

[9] Grasser T. Stochastic charge trapping in oxides: From random telegraph noise to bias temperature instabilities. Microelectron Reliab 2012;52(1):39–70. https://doi.org/10.1016/j.microrel.2011.09.002.

[10] Minimos-NT User Manual – Release 2018.04.

[11] Goes W, Wimmer Y, El-Sayed A-M, Rzepa G, Jech M, Shluger A, et al. Identification of oxide defects in semiconductor devices: a systematic approach linking DFT to rate equations and experimental evidence. Microelectron Reliab 2018;87:286–320. https://doi.org/10.1016/j.microrel.2017.12.021.

[12] Komsa H-P, Rantala TT, Pasquarello A. Finitesize supercell correction schemes for charged defect calculations. Phys Rev B 2012;86(4):1–16. https://doi.org/10.1103/PhysRevB.86.045112.

[13] Asenov A, Balasubramaniam R, Brown A, Davies J, Saini S. Random telegraph signal amplitudes in sub 100 nm (decanano) MOSFETs: a 3D 'Atomistic' simulation study. International Electron Devices Meeting 2000. Technical Digest. IEDM (Cat. No.00CH37138) IEEE; 2000. p. 279–82. https://doi.org/10.1109/IEDM.2000.904311.

[14] Asenov A, Brown A, Davies J, Kaya S, Slavcheva G. Simulation of intrinsic parameter fluctuations in decananometer and nanometer-scale MOSFETs. IEEE Trans Electron Devices Sep. 2003;50(9):1837–52. https://doi.org/10.1109/TED.2003.815862.

[15] Alexander C, Brown A, Watling J, Asenov A. Impact of scattering in 'atomistic' device simulations. Solid-State Electron May 2005;49(5):733–9. https://doi.org/10.1016/j.sse.2004.10.012.

[16] Jibin Z, Runsheng W, Shaofeng G, Mulong L, Zhuoqing Y, Xiaobo J, et al. New understanding of state-loss in complex RTN: statistical experimental study, trap interaction models, and impact on circuits. 2014 IEEE International Electron Devices Meeting IEEE; 2014. https://doi.org/10.1109/IEDM.2014.7047169. pp. 34.5.1–34.5.4.

[17] Gerrer L, Ding J, Amoroso S, Adamu-Lema F, Hussin R, Reid D, et al. Modelling RTN and BTI in nanoscale MOSFETs from device to circuit: a review. Microelectron Reliab 2014;54(4):682–97. https://doi.org/10.1016/j.microrel.2014.01.024.

[18] Asenov A, Slavcheva G, Brown A, Davies J, Saini S. Increase in the random dopant induced threshold fluctuations and lowering in sub-100 nm MOSFETs due to quantum effects: a 3-D density-gradient simulation study. IEEE Trans Electron Devices 2001;48(4):722–9. https://doi.org/10.1109/16.915703.

[19] Ancona MG, Iafrate GJ. Quantum correction to the equation of state of an electron gas in a semiconductor. Phys Rev B 1989;39(13):9536–40. https://doi.org/10.1103/PhysRevB.39.9536.

[20] Wettstein A, Schenk A, Fichtner W. Quantum device-simulation with the density-gradient model on unstructured grids. IEEE Trans Electron De vices 2001;48(2):279–84. https://doi.org/10.1109/16.902727.

[21] Conwell E, Weisskopf VF. Theory of impurity scattering in semiconductors. Phys Rev 1950;77(3):388–90. https://doi.org/10.1103/PhysRev.77.388.

[22] Alexander C, Roy G, Asenov A. Random-dopant-induced drain current variation in nano-MOSFETs: a three-dimensional self-consistent monte carlo simulation study using Ab initio ionized impurity scattering. IEEE Trans Electron Devices 2008;55(11):3251–8. https://doi.org/10.1109/TED.2008.2004647.

[23] Rossetto I, Bisi D, de Santi C, Stocco A, Meneghesso G, Zanoni E, et al. Performance-limiting traps in GaN-based HEMTs: from native defects to common impurities. In: Meneghini M, Meneghesso G, Zanoni E, editors. Power GaN Devices: Materials, Applications and Reliability Springer International Publishing; 2017. p. 197–236. https://doi.org/10.1007/978-3-319-43199-4_9.

[24] Ambacher O, Majewski J, Miskys C, Link A, Hermann M, Eickhoff M, et al. Pyroelectric properties of Al(In)GaN/GaN hetero- and quantum well structures. J Phys: Condens Matter 2002;14(13):3399.

[25] Miki H, Tega N, Yamaoka M, Frank DJ, Bansal A, Kobayashi M, et al. Statistical measurement of random telegraph noise and its impact in scaled-down high-_/metal-gate MOSFETs. 2012 International Electron Devices Meeting IEEE; 2012. https://doi.org/10.1109/IEDM.2012.6479071. pp. 19.1.1–19.1.4.

[26] Amoroso SM, Gerrer L, Adamu-Lema F, Markov S, Asenov A. Statistical study of bias temperature instabilities by means of 3D atomistic simulation. In: Grasser T, editor. Bias Temperature Instability for Devices and Circuits New York: Springer; 2014. p. 323–48. https://doi.org/10.1007/978-1-4614-7909-3_13.

[27] Hao P, Mao D, Wang R, Guo S, Ren P, Huang R. On the frequency dependence of oxide trap coupling in nanoscale MOSFETs: understanding based on complete 4-state trap model. 2016 13th IEEE International Conference on Solid-State and Integrated Circuit Technology IEEE; 2016. p. 981–3. https://doi.org/10.1109/ICSICT.2016.7998625.

[28] Guo S, Wang R, Mao D, Wang Y, Huang R. Anomalous random telegraph noise in nanoscale transistors as direct evidence of two metastable states of oxide traps. Scientific Rep Dec. 2017;7(1):6239. https://doi.org/10.1038/s41598-017-06467-7.

Alexander Grill studied Microelectronics at the Vienna University of Technology, where he received his Diplomingenieur degree in 2013. Since March 2013 he is working on his doctoral degree at the Institute for Microelectronics at TU Wien. His scientific interests are reliability modelling of Nitride based heterostructure devices with special focus on threshold voltage drift and the extraction of the physical properties of single defects.